

QUANTITATIVE CHARACTERISATION OF COMPLEX DEFECTS USING TWO-DIMENSIONAL ULTRASONIC ARRAYS

A. Velichko and P. D. Wilcox

Department of Mechanical Engineering, University of Bristol, Bristol, BS8 1TR, UK

1. Introduction

Recent years have seen a rapid increase in the interest in arrays for NDE. However, current NDE systems utilise mainly 1D arrays and so are limited to obtaining a 2D image. 2D arrays offer the potential to image in 3-dimensions. This has clear benefits as real defects and engineering structures are 3D – for example defects such as cracking and inclusions in welds are of arbitrary shape and can occur in arbitrary orientations. The 3D steering and focusing ability of 2D arrays enables both improved defect characterisation due to the increased range of inspection angles and increased volumetric coverage from a single inspection location. However there are a number of obstacles currently restricting the application of 2D arrays to NDE. The fundamental challenge associated with truly 2D arrays, capable of full 3D imaging, is due to the number of elements required to produce an aperture of sufficient size to allow adequate beam-forming. In this paper different techniques for optimization of 2D array element layout are presented.

2. Imaging strategy

2.1. Full matrix capture

The strategy of imaging using an ultrasonic array that is considered here consists of collecting signals from each transmitter-receiver pair in the array. Such an approach is called Full Matrix Capture and the acquired data contains all information about the test sample that could possibly be obtained by the array at a particular test position.

The next question is how to process this transmit-receive data in order to extract information about each defect. The imaging algorithms transform the array data into an image, which indicates the location of the defects in the sample. According to the distance between an array and the testing area it is possible to distinguish between two cases: near field imaging and far field imaging.

2.2. Near field imaging

In practice the near field of the array can be defined as:

$$D < L^2 / \lambda, \quad (1)$$

where D is the distance between reflector and the array, L is the linear size of the array aperture and λ is wavelength. In this case the reflector can be seen by the array from different angles and advanced methods for reflector characterization can be applied.

Any linear imaging algorithm can be written in the form

$$I(\mathbf{r}) = \sum_{\omega} \sum_{i,j} d_{ij}(\omega, \mathbf{r}) s_{ij}(\omega), \quad (2)$$

where indices i and j refer to the transmitter and receiver elements, respectively, $s_{ij}(\omega)$ is the frequency spectrum of array data, \mathbf{r} is the imaging point and d_{ij} are focusing coefficients.

One of the possible imaging techniques is the Total Focusing Method (TFM) [1], which is based on the delay-and-sum beam-forming. In this case the focusing coefficients are given by

$$d_{ij} = \exp(ik(R_{(T)i} + R_{(R)j})), \quad (3)$$

where $R_{(T)i}$ and $R_{(R)j}$ are the distances between transmitter/receiver positions to the imaging point, k is the wavenumber.

Apart from the TFM, there are some other imaging algorithms that can be applied for the near field imaging. For example, recently Fourier-domain approaches to full matrix imaging based on the wavenumber algorithm used in synthetic aperture radar and sonar [2] and the back-propagation of angular spectrum [3] have been developed. Although the Fourier-domain implementation of these methods requires the array elements to be configured in the form of rectangular grid, they can also be implemented using TFM type expression (2) with the equivalent focusing coefficients.

2.3. Far field imaging

The further a reflector is from an array, the smaller the range of angles it is illuminated over. If the distance between the array and reflector satisfies the following condition

$$D > L^2 / \lambda, \quad (4)$$

it is possible to consider that the reflector is seen by the array from approximately from one angle only. In the far field focusing is not possible and the imaging methods (2) only have the effect of beam steering. It will be shown below that in the far field, the performance of a fully populated array can be achieved by using sparse array.

2.4. Examples

Conditions (1) and (4) give an indication at what distance from the array the near and far field imaging can be applied. This distance depends on the array size and the wavelength of the excited signal. Below the estimation of the far field length for 1D and 2D arrays are given. It is assumed that the operating frequency is 3 MHz or 5 MHz and the wave velocity in the test sample is 6000 ms^{-1} . The length of the longitudinal bulk wave at these frequencies is 2 mm and 1.2 mm, respectively.

It is assumed that the array controller has 128 parallel channels. This results in a maximum of 128 independent array elements. For a 1D linear array with 128 elements with the element pitch equal to the half of the wavelength the formula (4) gives far-field values of about 8 m for the 3 MHz array and 5 m for the 5 MHz array. Therefore, in the case of the 1D array all measurements are in the near field in practical applications.

The total number of the elements in the 2D matrix array is N^2 , where N is the number of elements in one row. Hence, using the array controller with 128 channels the maximum $11^2 = 121$ element matrix array can be operated. If the half wavelength element pitch is taken then the array size is $L = 11 \text{ mm}$ at 3 MHz and $L = 6.6 \text{ mm}$ at 5 MHz centre frequency. In this case the far field imaging is possible at distances $D > 60 \text{ mm}$ for the 3 MHz array and $D > 36 \text{ mm}$ for the 5 MHz array. These results show that for the 2D array the far field imaging has potential practical applications.

3. Far field imaging

3.1. Far field approximation

It is assumed that the transmitter and receiver elements are located at the points $\mathbf{r}_{(T)i}$ and $\mathbf{r}_{(R)j}$, respectively and that the coordinate origin is the centre of the array. If all reflectors are situated in the far-field of the whole array, then the distances $R_{(T)i}$ and $R_{(R)j}$ can be approximately written as

$$R_{(T)i} \approx r - \mathbf{r}_{(T)i} \cdot \mathbf{n}, \quad R_{(R)j} \approx r - \mathbf{r}_{(R)j} \cdot \mathbf{n}, \quad (5)$$

where $\mathbf{n} = \mathbf{r}/r$ is a unit vector pointing from the array to the imaging point. The expression (4) for the image can be rewritten in the form

$$I(\mathbf{n}, r) = \sum_{\omega} A(\omega, \mathbf{n}) \exp(2ikr), \quad (6)$$

$$A(\omega, \mathbf{n}) = \sum_m s_m(\omega) d_m(\omega, \mathbf{n}), \quad (7)$$

$$d_m = \exp(ik\mathbf{r}_m \mathbf{n}), \quad \mathbf{r}_m = \mathbf{r}_{(T)i} + \mathbf{r}_{(R)j}. \quad (8)$$

In formula (7) the index “m” changes from 1 to $N=N_T N_R$, where N_T and N_R are number of transmitter and receiver elements in the array.

The processing algorithm can be divided into two parts. The first part is defined by expression (7) and is associated with angular resolution. The function A represents the reflected signal from the \mathbf{n} direction. The second part is the determination of the function I as a function of the radial distance r for each direction and is defined by the expression (6). This step is associated with radial resolution.

The quality of the angular resolution can be characterized by the Point Spread Function (PSF). The PSF $P(\mathbf{n}, \mathbf{n}_0)$ is the result for a point reflector located at the direction \mathbf{n}_0 and can be written as

$$P(\mathbf{n}, \mathbf{n}_0) = \sum_m d_m(\mathbf{n}) \exp(-ik\mathbf{r}_m \mathbf{n}_0), \quad (9)$$

3.2. Effective aperture

Expression (9) is equivalent to the far field angular pattern produced by the system of virtual transmitters located at the points \mathbf{r}_m . Therefore the angular resolution of the real array is equivalent to the transmit beam pattern of an effective aperture of transmitters located at the points \mathbf{r}_m . For example, for a rectangular array with elements around the perimeter that act as transmitters and receivers, the equivalent transmitter array is a rectangular matrix array with an aperture of twice the size that is fully populated with elements. For a circular array with transducers around the perimeter only, the equivalent transmitter array consists of a circular area of twice the diameter densely populated with elements.

Note, that for a fully populated transmitter-receiver array the effective array is the same as for a sparse array with the elements located along the perimeter of the original array. This means that in the far field performance of fully populated array can be achieved by using sparse array.

From the theory of phased arrays it is well known that the beamforming can be significantly improved by applying element weights d_m in the sum (7) different from the phase addition coefficients given by the expression (8). To calculate these optimal focusing coefficients different known methods of pattern synthesis for phased arrays can be applied. One possible approach consists in following. Consider firstly the fully populated array with elements uniformly distributed over array aperture. In this case the summation in (9) can be replaced by the integral over the area D of the array:

$$P(\mathbf{n}, \mathbf{n}_0) = \iint_D d(\boldsymbol{\rho}, \mathbf{n}) \exp(-ik\boldsymbol{\rho} \mathbf{n}_0) d\boldsymbol{\rho}, \quad (10)$$

It is clear that good focusing can be obtained using the weights

$$d(\boldsymbol{\rho}, \mathbf{n}) = G(\rho) \exp(ik\boldsymbol{\rho} \mathbf{n}), \quad (11)$$

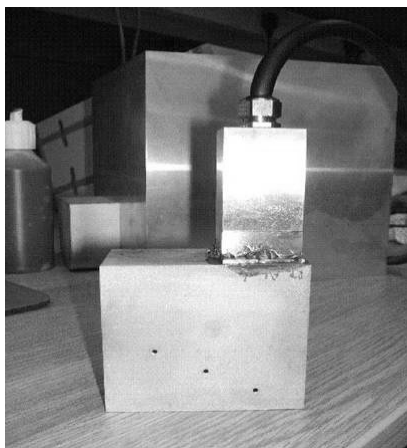
where $\rho=|\boldsymbol{\rho}|$ and the function G represent Gaussian apodization.

If the array consists of finite number of separate elements then the sum in (9) can be considered as a discrete approximation to the integral (10). The element weights can be corrected based on the position \mathbf{r}_m of the effective element and the correction factor g_m is determined by the cubature formula. For the rectangular array the elements distribution in the effective array is uniform and, so, $g_m=1$. For the circular array the element density in the effective array is nonuniform and depends on the distance of the element form the array centre.

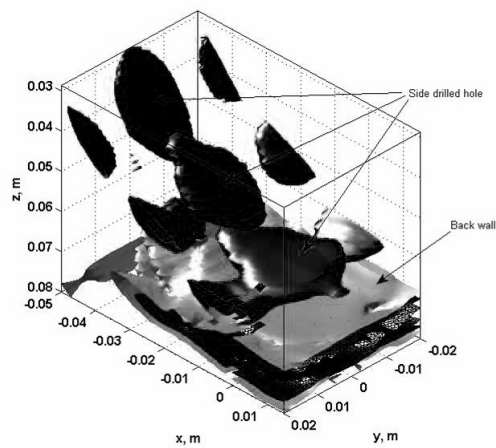
3.3. Demonstration of Effective Aperture Far Field Imaging of Side Drilled Holes

A 11x11 2D matrix array manufactured by Imasonic, France with 3-MHz centre frequency was used on an aluminium block with dimensions 40x70x70 mm and with 3 side drilled through holes of diameter 1.5 mm at different depths as shown in Fig. 1(a). Here the distance of the holes to the centre of the array is approaching that which would be regarded as being in the far-field. Therefore, this is a suitable configuration to compare far-field imaging using the full array and far-field imaging using only the perimeter elements of the array (i.e. a sparse array). A 3D image obtained using the far-field TFM applied to all elements in the array is shown in Fig. 1(b). As in the previous example, the side drilled holes each appear as three signals, one from the specular reflection from the middle of the hole below the array and two reflections from the hole ends.

Because far-field imaging is effectively beam steering, the natural coordinates for 2D images are those of a 3D sector scan (i.e. range, r , azimuth angle, ϕ , and elevation angle, θ). Results for three different imaging methods are shown in Fig. 2. In each sub-figure in Fig. 2, two images are presented: one in the r - θ plane passing through the mid-plane of the sample and the second on an θ - ϕ hemisphere at a constant value of r chosen to include the specular reflection from the side-drilled hole directly below the array. Note that because the imaging plane in the right hand images is hemispherical the signals from the ends of the hole of interest are not visible as there do not lie in this plane; however, indications of the signals from the ends but not the centre of another hole are clearly visible as for this sample these do happen to lie on the hemisphere. Fig. 2(a) shows the images obtained from applying the far-field TFM to data from all elements in the array (i.e. these are cross sections through Fig. 1(b)) and provide the benchmark for other images. Fig. 2(b) shows the images obtained when the far-field TFM is applied to data obtained from the 40 elements around the perimeter of the array only. It can be observed that while the main specular reflection from the hole is still clearly visible, there are now major sidelobes corrupting the image. Fig. 2(c) shows the results of reprocessing the data from the perimeter elements using the effective aperture technique with Gaussian apodisation. This provides a significant improvement in image quality over the previous image.



(a)



(b)

FIGURE 1. (a) Experimental arrangement test on aluminium block 40x40x70mm with 3 through holes and (b) -40 dB isosurface image obtained using TFM applied to data from all elements in array.

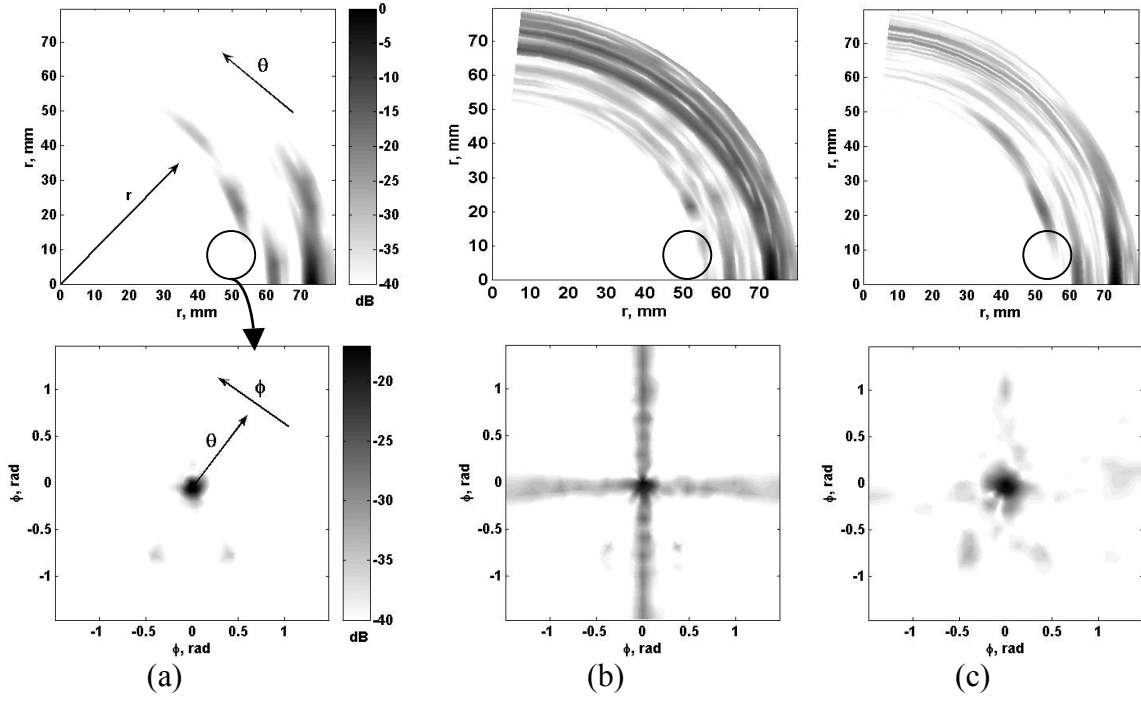


FIGURE 2. Far-field images of aluminium block 40x40x70mm with 3 through holes: (a) TFM, full array (121 elements) ; (b) TFM, sparse rectangular array (40 elements); (c) Effective aperture compensation, sparse array rectangular array (40 elements). The first image in each column is in the vertical r - θ plane at $\phi = 0$, the second image is an θ - ϕ hemisphere at $r = 60$ mm.

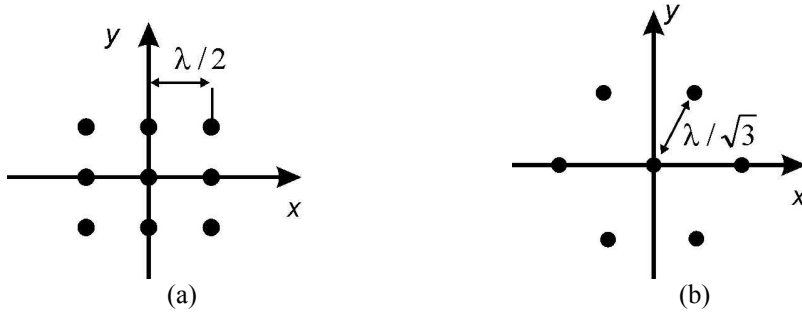


FIGURE 3. (a) Rectangular sampling; (b) Hexagonal sampling.

4. Near field imaging

4.1. Optimization of array layout

The array data s_{ij} represent samples of the transmitted and received wavefield $s(\mathbf{r}_{(T)i}, \mathbf{r}_{(R)j})$. The best performance of the array can be achieved if the function $s(\mathbf{r}_{(T)}, \mathbf{r}_{(R)})$ can be reconstructed from its sample values s_{ij} , otherwise there is loss of information. In the previous section it has been shown that if the scatterer is in the far-field of the array then the function s depends only on one variable $\mathbf{r}_{(T)} + \mathbf{r}_{(R)}$ and its reconstruction can be performed using sparse array. If the scatterer is in the near-field of the array then the function s is an arbitrary bandlimited function. In this case the problem of optimum element layout can be formulated as follows: what is the most efficient sampling scheme requiring the minimum number sampling points per unit area for reconstruction a continuous bandlimited 2D function?

4.2. Regular sampling

The most straightforward generalization of the 1D regular sampling to the 2D case is rectangular sampling schematically shown in Fig.3a. Any regular (i.e. periodic) sampling pattern has corresponding sampling criterion. If the distance between sampling points is greater than some maximum allowable value then high-frequency components of the function s appear as low-frequency components of the reconstructed function. This effect is called aliasing. In order to avoid aliasing the spacing between sampling points in rectangular pattern must be less than $\lambda/2$.

However, in the 2D case (in contrast with the 1D case) there is infinite number of other possible regular sampling patterns. It can be shown [4], that the optimum sampling scheme with the lowest density of sampling points is hexagonal sampling. The elements are located on a triangular grid as shown in Fig.3b and the element spacing is $\lambda/\sqrt{3}$.

To quantify the advantage of the hexagonal pattern over the rectangular pattern the array controller with 128 parallel channels is considered. Using rectangular sampling the maximum square matrix array has $11^2 = 121$ elements. On the other hand, the same array aperture and, hence, the same imaging performance can be achieved with a hexagonal array of 91 elements. Alternatively, by using the maximum possible number of elements in a hexagonal formation (which results in a 127 element array) the linear size of array can be increased by 20% relative to the 11x11 element rectangular array.

4.3. Non-uniform sampling

If the sampling criterion for the regular sampling scheme is not satisfied then the reconstructed function contains aliasing peaks. As a result the grating lobes appear in the image. Note that these localized artifacts are caused by the periodicity of the array element layout only. Irregular distribution of the array elements suppresses aliasing peaks but at the expense of increased uniform noise throughout image. The problem of finding the optimal non-uniform sampling distribution is well known in Computer Graphics [5]. One of the best solutions is a Poisson disk distribution – random element locations with constraint on minimum separation distance. Interestingly, the distribution of the photoreceptors in a human eye is a Poisson disk distribution [6].

The limiting factor in using irregular sampling pattern is how high a uniform noise level can be tolerated in the image. In order to illustrate the performance of non-uniform array, the following modeling example is considered. It is assumed that the center frequency is 5 MHz and the wavelength at this frequency is $\lambda = 1.3$ mm. 7 point scatterers are placed at the distance $z = 15$ mm from the array as shown in Fig.4a. In Fig.4b-d isosurfaces at -37 dB of 3D images obtained by the TFM for 3 different array configurations are shown. Fig. 4b shows the result for a hexagonal array with 127 elements and an element pitch of $\lambda/\sqrt{3}$, which satisfies to the sampling criterion. Fig. 4c corresponds to a hexagonal array with an element pitch of $2\lambda/\sqrt{3}$. Fig. 4d shows the image for 128 element array with the Poisson disk element distribution. As expected, larger array aperture due to increased element pitch leads to higher resolution. However, in the case of hexagonal sampling this is accompanied by localized grating lobes. On the other hand, all grating lobes are significantly suppressed by using non-uniform sampling.

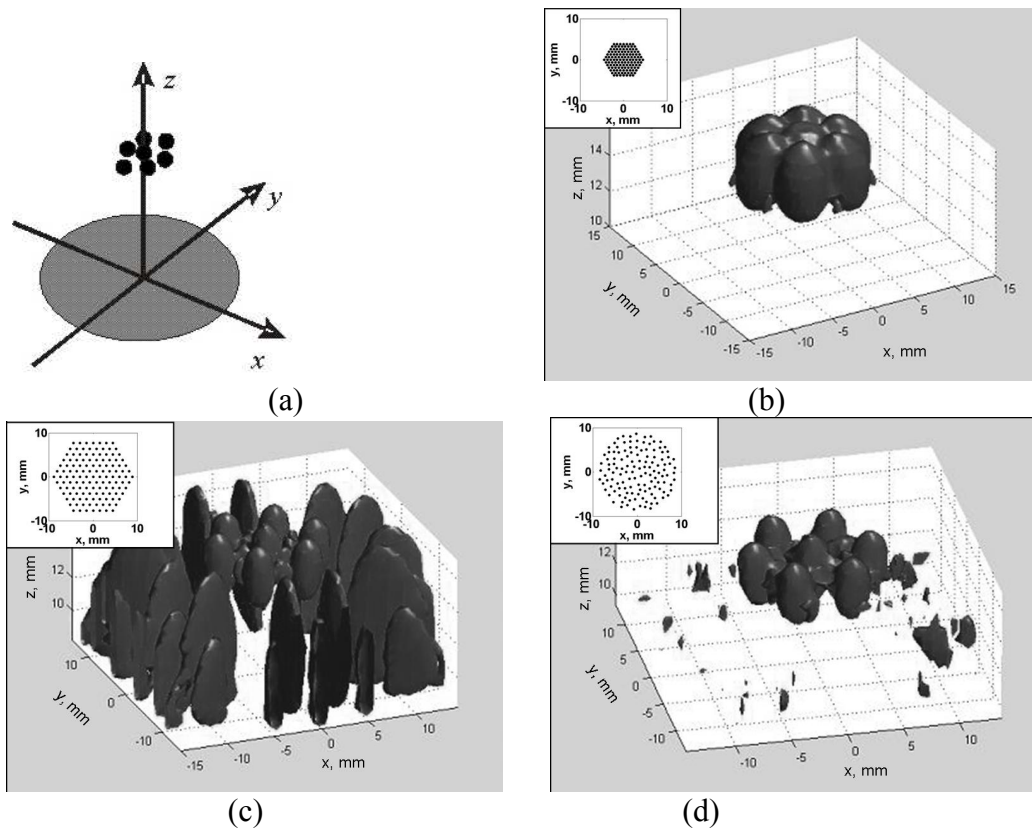


FIGURE 4. (a) Geometry of modeling example. 3D images (isosurfaces at -37 dB) for (b) hexagonal array layout, element pitch corresponds to the sampling criterion, (c) hexagonal array layout, element pitch is twice the sampling criterion, (d) Poisson disk element distribution; insets show the array layouts.

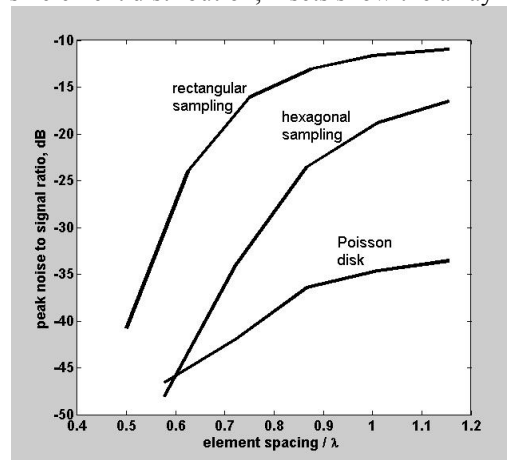


FIGURE 5. Peak noise to signal ratio as a function of the element pitch for rectangular, hexagonal and Poisson disk sampling schemes.

The peak noise to signal ratio as a function of the element pitch for rectangular, hexagonal and Poisson disk sampling schemes is presented in Fig. 5. In this case one point scatterer was placed at $x = 10$ mm, $y = 0$, $z = 15$ mm. It can be seen that, to keep the noise level below -35 dB, the Poisson disk configuration enables the mean element pitch to be made approximately twice as big as the best regular configuration (hexagonal).

5. Summary

The problem of the optimum 2D array layout has been considered. It has been shown that in the case of the far-field imaging the performance of fully populated array can be achieved by using sparse array. For the near-field imaging and regular array pattern hexagonal elements on a triangular grid is optimum (about 20% more efficient than square elements on

square grid). Increasing of separation distance between array elements leads to grating lobes in the image. However, a random distribution of array elements suppresses localized grating lobes but at the expense of increased uniform noise throughout the image.

Acknowledgements

This work was supported by the UK Engineering and Physical Sciences Research Council (grant no. EP/F005032/1) through the UK Research Centre in NDE and by Airbus, the National Nuclear Laboratory, Rolls-Royce, Serco Assurance and Shell.

References

1. B. W. Drinkwater and P. D. Wilcox, *NDT&E Int.*, **39**(7), 525-541 (2006).
2. A.J. Hunter, B.W. Drinkwater and P.D. Wilcox, *IEEE Trans. Ultrason., Ferroelect., Freq. Contr.*, **55**(11), pp. 2450-2462 (2008).
3. A. Velichko and P.D. Wilcox, in *Review of Progress in QNDE*, **28**, edited by D. O. Thompson and D. E. Chimenti, American Institute of Physics, Melville, NY (2009), pp. 634-641.
4. D. P. Petersen and D. Middleton, *Information and Control*, **5**, (1962), pp. 279-323.
5. R.L. Cook, *ACM Trans. Graphics*, **5**(1), (1986), pp. 51-72.
6. J.I. Yellott, *Science*, New Series, **221**(4608) (1983), pp. 382-385.